university of groningen

University Medical Center Groningen

University of Groningen

Direct visualization of magnetoelectric domains

Geng, Yanan; Das, Hena; Wysocki, Aleksander L.; Wang, Xueyun; Cheong, S-W.; Mostovoy, M.; Fennie, Craig J.; Wu, Weida

Published in:
Nature Materials

DOI:
10.1038/nmat3813

IMPORTANT NOTE: You are advised to consult the publisher's version (publisher's PDF) if you wish to cite from it. Please check the document version below.

Document Version
Publisher's PDF, also known as Version of record

Publication date:
2014

Link to publication in University of Groningen/UMCG research database

Citation for published version (APA):
Geng, Y., Das, H., Wysocki, A. L., Wang, X., Cheong, S-W., Mostovoy, M., Fennie, C. J., & Wu, W. (2014). Direct visualization of magnetoelectric domains. *Nature Materials*, *13*(2), 163-167. https://doi.org/10.1038/nmat3813

Copyright
Other than for strictly personal use, it is not permitted to download or to forward/distribute the text or part of it without the consent of the author(s) and/or copyright holder(s), unless the work is under an open content license (like Creative Commons).

The publication may also be distributed here under the terms of Article 25fa of the Dutch Copyright Act, indicated by the "Taverne" license. More information can be found on the University of Groningen website: https://www.rug.nl/library/open-access/self-archiving-pure/taverne-amendment.

Take-down policy
If you believe that this document breaches copyright please contact us providing details, and we will remove access to the work immediately and investigate your claim.

Downloaded from the University of Groningen/UMCG research database (Pure): http://www.rug.nl/research/portal. For technical reasons the number of authors shown on this cover page is limited to 10 maximum.

Download date: 05-05-2023

nature materials

LETTERS

PUBLISHED ONLINE: 1 DECEMBER 2013 | DOI: 10.1038/NMAT3813

Direct visualization of magnetoelectric domains

Yanan Geng[1], Hena Das[2], Aleksander L. Wysocki[2], Xueyun Wang[1], S-W. Cheong[1], M. Mostovoy[3], Craig J. Fennie[2] and Weida Wu[1]*

The coupling between the magnetic and electric dipoles in multiferroic and magnetoelectric materials holds promise for conceptually novel electronic devices[1–3]. This calls for the development of local probes of the magnetoelectric response, which is strongly affected by defects in magnetic and ferroelectric ground states. For example, multiferroic hexagonal rare earth manganites exhibit a dense network of boundaries between six degenerate states of their crystal lattice, which are locked to both ferroelectric and magnetic domain walls. Here we present the application of a magnetoelectric force microscopy technique that combines magnetic force microscopy with *in situ* modulating high electric fields. This method allows us to image the magnetoelectric response of the domain patterns in hexagonal manganites directly. We find that this response changes sign at each structural domain wall, a result that is corroborated by symmetry analysis and phenomenological modelling[4], and provides compelling evidence for a lattice-mediated magnetoelectric coupling. The direct visualization of magnetoelectric domains at mesoscopic scales opens up explorations of emergent phenomena in multifunctional materials with multiple coupled orders.

The magnetoelectric effect, first discussed by Landau and Lifshitz, has an outstanding history in condensed matter physics beginning with Dzyalochinskii's seminal prediction of the effect in Cr_2O_3 that was quickly confirmed by experiments[5–7]. The potential applications in data storage and sensors had generated an intensive research interest in magnetoelectric materials throughout the 1970s (refs 8,9). The revival of magnetoelectricity in the past decade has been fuelled by the discoveries of new multiferroic materials exhibiting giant magnetoelectric effects due to the cross-coupling between the coexisting ferroelectric and magnetic orders[9–11]. Recently, the quantized magnetoelectric polarizability has been proposed to classify three-dimensional topological insulators in the presence of strong correlations[12,13]. Therefore, the magnetoelectric effect has a profound and broad impact on diverse areas of materials science.

Although sensitive techniques have been developed for macroscopic measurements of magnetoelectric effects, little has been done on mesoscopic detection of such an effect within a single domain or at domain walls[14]. Macroscopic magnetoelectric measurements also require preparations of a single-domain state, which could be problematic for many materials[15–17]. On the other hand, the coupled ferroelectric and magnetic domains or walls are the key to understand the mechanisms of the giant responses in many multiferroics[17–20]. Furthermore, understanding and controlling domains and domain walls is critical for using any ferroic material in technological applications. Therefore, it is of both fundamental and practical interest to directly visualize magnetoelectric domains or domain walls. Some efforts on visualizing electric-field-induced changes of local magnetic configuration have been reported[21], yet the direct detection of magnetoelectric coupling within a domain or at the domain wall is still lacking. Here, we demonstrate a microscopy technique we call magnetoelectric force microscopy (MeFM), which is a combination of magnetic force microscopy (MFM) and *in situ* modulated electric fields (**E**), and can be employed to detect the **E**-induced magnetization ($\mathbf{M}_E$), as illustrated in Fig. 1. Using MeFM, we directly observed the local, intrinsic bulk magnetoelectric response of each multiferroic domain in hexagonal (*h*-) $ErMnO_3$, in excellent agreement with a symmetry analysis, a microscopic model and first-principles calculations[4]. Furthermore, a giant enhancement of the magnetoelectric response was observed in the proximity of a critical point below 2 K, suggesting that critical fluctuations of competing orders may be harnessed for colossal **E**-induced magnetic responses.

Figure 1 shows the basic principle of the MeFM, which can be summarized as a lock-in detection of $\mathbf{M}_E$. The top electrode (a thin metal film deposited on the sample surface) was grounded to screen all **E**-fields. A modulated voltage $V(\omega)$ is applied to the bottom electrode to generate a modulated **E**-field across the sample. If the linear magnetoelectric tensor (α) is non-zero, this results in a magnetic stray field $B(\omega)$ proportional to $M_E(\omega)$. $B(\omega)$ is sensed by a MFM tip lifted from the surface, producing a modulated MFM signal $\delta f(\omega)$ (the change of the resonant frequency of the cantilever) that is extracted by a phase-locked loop[20]. The $\delta f(\omega)$ signal is then fed to a lock-in amplifier to extract δf, which we refer to as the MeFM signal. A MeFM image is generated by recording the MeFM signal at every pixel. As MFM is sensitive only to the out-of-plane component of the magnetic stray field, the MeFM signal corresponds to the diagonal component of α. Our MeFM technique is demonstrated by imaging the magnetoelectric response of multiferroic domains in *h*-$ErMnO_3$ single crystals. In addition, we have performed several control experiments to exclude possible extrinsic origins of MeFM signals (Supplementary Discussion 1 and Figs 1–3).

The *h*-$REMnO_3$ (RE—rare earths) compounds[22,23] are improper ferroelectrics[24,25] in which the polarization (**P**) is induced by a structural instability called the trimerization mode ($\mathbf{Q}_{K_3}$) that condenses at $T_c \sim 1{,}300$–$1{,}500$ K. The Mn^{3+} spins form a 120° non-collinear antiferromagnetic order (**L**) in the crystallographic *xy*-plane below the Néel temperature ($T_N \approx 70$–90 K; ref. 26). The nonlinear coupling between **P** and $\mathbf{Q}_{K_3}$ modes results in six-state topological vortices with interlocked ferroelectric and structural anti-phase domain walls[16,25,27], where a net magnetization was discovered in *h*-$ErMnO_3$ (ref. 20). Although the magnetization is only non-zero at the domain wall, its appearance is a direct manifestation of a strong and non-trivial bulk coupling of **L**, **P**

[1]Department of Physics and Astronomy and Rutgers Center for Emergent Materials, Rutgers University, Piscataway, New Jersey 08854, USA, [2]School of Applied and Engineering Physics, Cornell University, Ithaca, New York, 14853, USA, [3]Zernike Institute for Advanced Materials, University of Groningen, Nijenborgh 4, 9747 AG, Groningen, The Netherlands. *e-mail: wdwu@physics.rutgers.edu

© 2014 Macmillan Publishers Limited. All rights reserved

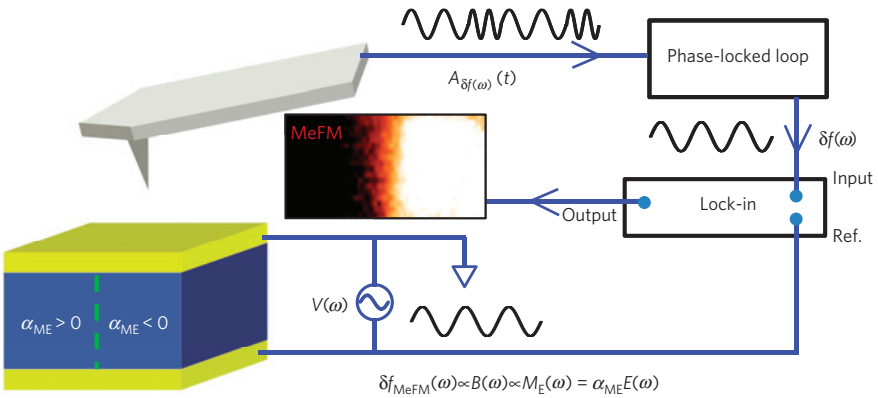

Figure 1 | Schematic of MeFM set-up. The basic principle of MeFM is the lock-in detection of the demodulated MFM signal from the **E**-field-induced magnetization ($\mathbf{M}_E$). A modulated voltage $V(\omega)$ is applied to the bottom electrode to generate a modulated electric field $E(\omega)$. The non-zero magnetoelectric effect (α) results in a magnetic stray field $B(\omega)$ proportional to the induced magnetization $M_E(\omega)$. $B(\omega)$ is detected by MFM, producing a modulated MFM signal $\delta f(\omega)$. Here $A_{\delta f(\omega)}(t)$ is the cantilever oscillation amplitude. The MFM signal is demodulated by a lock-in amplifier to extract δf, that is, the MeFM signal. The domains with different magnetoelectric coefficients would have different image contrast.

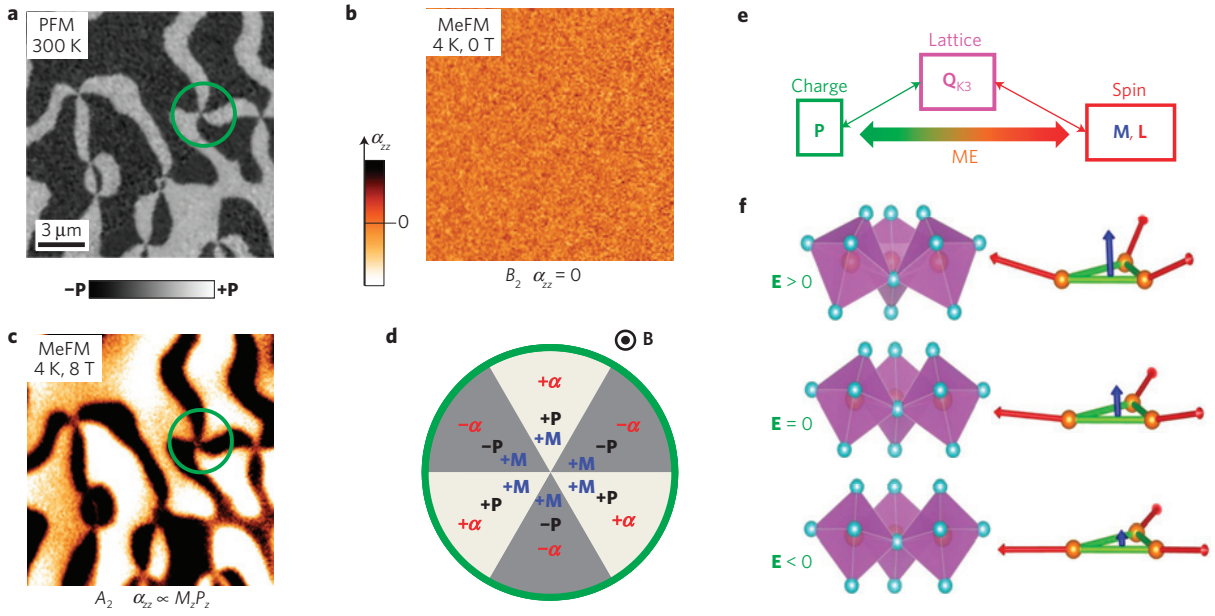

Figure 2 | MeFM results of h-ErMnO$_3$. a–c, Room-temperature PFM image (**a**), and low-temperature (4 K) MeFM images at zero magnetic field (**b**) and 8.0 T (**c**), were taken at the same location on the (001) surface of a *h*-$ErMnO_3$ single crystal. The white (dark) colour in the PFM image represents an up (down) ferroelectric domain. **d**, A cartoon of the magnetoelectric coefficient ($\boldsymbol{\alpha}_{zz}$) of the A_2 phase in different ferroelectric domains in *h*-$ErMnO_3$. **e**, A cartoon of the effective magnetoelectric coupling through structural instability trimerization. **f**, Cartoons of the changes of the buckling of MnO_5 polyhedra (trimer mode $\mathbf{Q}_{K3}$) induced by **E**-fields through **P** resulting in the changes of the canting moment **M** of Mn^{3+} spins.

and $\mathbf{Q}_{K_3}$ within each domain[4,20,25,28]. The same coupling can give rise to a bulk linear magnetoelectric effect if the magnetic structure of the domain wall could be realized throughout the domain. This is, in fact, possible to do by applying a strong magnetic field (**H**), which induces a transition from the B_2 ($P\underline{6}_3\underline{c}m$) phase to the A_2 ($P\underline{6}_3\underline{c}m$) phase that emerges at the domain walls in the B_2 phase[25]. Our MeFM technique allows for the first time a direct visualization of the resulting magnetoelectric domains, which we now discuss.

The ferroelectric domain pattern on the (001) surface of *h*-$ErMnO_3$ was visualized with piezo-response force microscopy (PFM) at room temperature. The resulting image (Fig. 2a) shows the network of ferroelectric domains coinciding with structural domains, which explains the origin of the clearly visible six-fold vortex structures. Using topographic features as alignment marks, MeFM images were taken at the same location[20]. In zero magnetic field, the Mn^{3+} spins order in a 120° pattern with magnetic symmetry $P\underline{6}_3\underline{c}m$ (B_2), which forbids any linear magnetoelectric effect[8]. Consistently, no MeFM contrast was observed in zero magnetic field at 4 K (Fig. 2b) with $E = 10\,\mathrm{kV\,cm^{-1}}$. The spin configuration of the *h*-$ErMnO_3$ can be controlled with the application of a magnetic field along the *z* axis[26]. In a large field, an A_2 ($P\underline{6}_3\underline{c}m$) phase, which allows diagonal components of α, emerges from the B_2 ground state[8,29]. In the A_2 phase, the in-plane Mn^{3+} spins rotate through 90° from that of the B_2 phase, resulting in a net magnetic moment (M_z) along the *z* axis due to canting of spins of Mn^{3+} ions. We, indeed, observed a sharp MeFM contrast in 8 T at 4 K (Fig. 2c) with $E = 10\,\mathrm{kV\,cm^{-1}}$. The sign of the MeFM signal changes at ferroelectric domain walls, that is, the magnetoelectric domain pattern is identical to the

© 2014 Macmillan Publishers Limited. All rights reserved

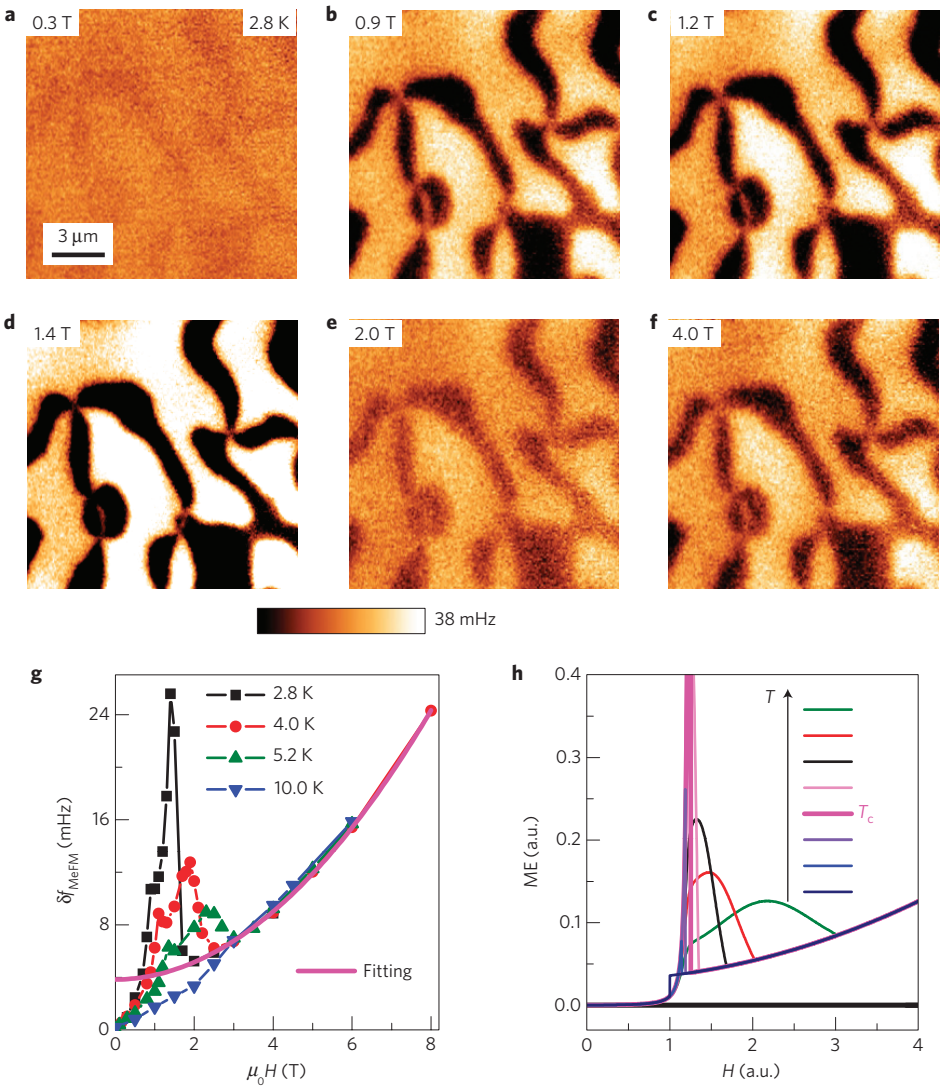

Figure 3 | MeFM images and the *H*-dependence of the MeFM signal. a–f, The representative MeFM images taken at 2.8 K in various magnetic fields. All of the images are in the same colour scale. **g**, *H*-dependence of the MeFM signal at 2.8, 4.0, 5.2 and 10 K, respectively. The solid curve (magenta) is the polynomial fitting MeFM(H) $= a + c \cdot (\mu_0 H)^2$ of the high-field A_2 phase with extrapolation to zero field. The intercept (a) of the fitting curve corresponds to the linear magnetoelectric effect in the A_2 phase. **h**, The simulated magnetic field (H) dependence of magnetoelectric responses at various effective temperatures (T) using a phenomenological Landau theory of the reorientation transition. Here T_c is the critical temperature at which the order of the spin reorientation transition changes from second to first (see Supplementary Discussion 5).

ferroelectric one (Fig. 2d), suggesting $\alpha_{zz} \propto M_z P_z$. Here the dark (bright) colour in MeFM images corresponds to domains with $+\alpha_{zz}$ ($-\alpha_{zz}$). We observed similar MeFM results on h-$ErMnO_3$ crystals with a stripe domain pattern (Supplementary Fig. 3). Furthermore, our MeFM signal changed its sign in reversed magnetic fields, confirming $\alpha_{zz} \propto M_z P_z$ (Supplementary Fig. 4). Therefore, our MeFM technique is capable of detecting local magnetoelectric effects at the mesoscopic scale in a situation where a macroscopic measurement, performed, for example, by making a capacitor structure, would be complicated by the averaging of the effect due to the presence of magnetoelectric domains.

In the A_2 phase, M_z originates from anisotropic Dzyaloshinskii–Moriya interactions between neighbouring Mn^{3+} spins[4]. A symmetry analysis shows that $M_z \propto \mathbf{L}_{A_2} \cdot \mathbf{Q}_{K_3}$, where $\mathbf{L}_{A_2}$ is the magnetic order parameter describing the symmetry of the A_2 phase (Supplementary Fig. 5). As $P_z \propto Q_{K_3} \cos 3\Phi$ at $T \ll T_c$ (ref. 24), the trimer mode ($\mathbf{Q}_{K_3}$) mediates an effective cross-coupling between P_z and M_z($\mathbf{L}_{A_2}$), that is, a linear magnetoelectric effect (Fig. 2e). This effect can also be understood in terms of a simple phenomenological free-energy expansion $f^{ME} \propto \cos(3\Phi) L_{A_2} E_z H_z$ derived from a symmetry analysis (Supplementary Fig. 5 and Discussion 2), giving $\alpha_{zz} \propto \cos(3\Phi) L_{A_2} \propto M_z P_z$, which is in excellent agreement with our experimental observation and the recent microscopic model[4]. Qualitatively, the **E**-field induces changes of $\mathbf{Q}_{K_3}$ through **P**, leading to changes of $\mathbf{M}_z$ (Fig. 2f and Supplementary Discussion 2). The excellent agreement between our MeFM results and the microscopic model provides compelling evidence for the fundamental mechanism of lattice-mediated magnetoelectric couplings, which may be generalized to other materials[4,30].

In addition, our systematic MeFM studies at various temperatures (2.8–10 K) and magnetic fields (0–8 T) reveal a giant enhancement of the magnetoelectric effect. Figure 3a–f shows representative MeFM images taken at 2.8 K in various magnetic fields (complete data in Supplementary Fig. 7). Overall, the MeFM contrast increases with increasing magnetic field. Surprisingly, the contrast is strongest at ~1.4 T, indicating a non-monotonic field dependence

© 2014 Macmillan Publishers Limited. All rights reserved

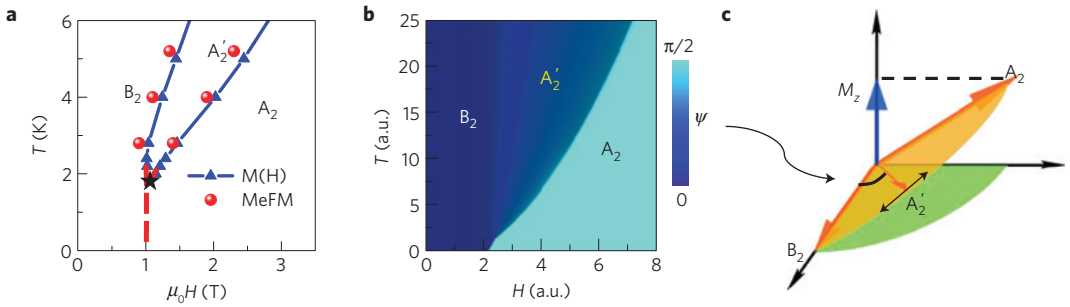

Figure 4 | *T*–*H* phase diagram and a cartoon of critical fluctuation in the A_2' phase. a, The *T*–*H* phase diagram of *h*-$ErMnO_3$ constructed from the anomalies in MeFM (red spheres) and in d*M*/d*H* data (blue triangles) at various temperatures. The two crossovers converge into a possibly critical point (the black star) of a first-order phase transition of $B_2 \rightarrow A_2$ (the red dashed line) below 2 K. **b**, A simulated *T*–*H* phase diagram using a phenomenological Landau theory (see Supplementary Discussion 5). The colour contrast represents the order parameter (the angle of Mn^{3+} spin) ψ ranging from 0 (B_2) to $\pi/2$ (A_2). The continuous (second order) spin reorientation transition in the A_2' region becomes an abrupt jump (that is, first order) below the tri-critical point. **c**, A cartoon illustration of giant responses due to critical fluctuations of Mn^{3+} spins in the intermediate A_2' phase near the critical point of the transition from the B_2 phase ($M_z = 0$) to the A_2 phase ($M_z \neq 0$). The canting angle of Mn^{3+} spins is exaggerated for illustration.

of the magnetoelectric effect. More quantitative information can be obtained by plotting the MeFM contrast (the difference between neighbouring domains) as a function of magnetic field ($\mu_0 H$) measured at various temperatures (2.8, 4.0, 5.2 and 10.0 K), as shown in Fig. 3g. The *H*-dependence of MeFM data can be approximately divided into three different intervals: the high-field ($\mu_0 H > 2$–3 T) A_2 region, the low-field ($0 < \mu_0 H < 1$ T) B_2 region and the intermediate-field (1 T $< \mu_0 H <$ 2–3 T) A_2' region.

In the A_2 region, the MeFM signal is approximately *T*-independent below 10 K, that is, all of the high-field data points collapse to a single curve described by $\mathrm{MeFM}(H) = a + c \cdot (\mu_0 H)^2$ (solid line in Fig. 3g), which is consistent with the A_2 magnetic symmetry and the saturation of both Mn^{3+} and Er^{3+} ordered moments at $T \ll T_N (\sim 80\,\mathrm{K})$. Here *a* and *c* are the fitting parameters. The intercept (*a*) is proportional to α_{zz} originating from the $L_{A_2} E_z H_z$ term in the free-energy expansion, and the second part is the nonlinear magnetoelectric coefficient due to the $L_{A_2} E_z H_z^3$ term in free energy (Supplementary Discussion 5). This behaviour is more apparent when plotting the MeFM signal versus H^2 (Supplementary Fig. 8). This suggests that the linear magnetoelectric effect dominates at low fields, whereas the nonlinear one prevails at high magnetic fields. By calibrating the MFM tip using known magnetic materials, we obtained an estimate of the measured linear magnetoelectric coefficient $\alpha_{zz}^{\mathrm{exp}} \sim 13\,\mathrm{ps\,m^{-1}}$, which is in reasonable agreement with that estimated from first-principles calculations ($\alpha_{zz}^{\mathrm{th}} \sim 0.7\,\mathrm{ps\,m^{-1}}$), where only the contribution of Mn^{3+} spins is taken into account (Supplementary Discussion 2 and 3 and Figs 6 and 9)[4]. This indicates that the strong spin–orbital coupling from rare-earth elements may enhance α_{zz} in the A_2 phase. Our results are also consistent with the previous macroscopic magnetoelectric measurements ($\alpha_{zz} \sim 3\,\mathrm{ps\,m^{-1}}$) on (partially) poled *h*-$ErMnO_3$ single crystals[31]. In the B_2 region, $\mathrm{MeFM}(H) = b \cdot (\mu_0 H)$, corresponding to the $E_z H_z^2$ term in the free energy. Here *b* is the fitting parameter. Interestingly, the low-field MeFM data collapse to a single curve with the H/T scaling, indicating that it may originate from the paramagnetic moments of, for example, Er^{3+} spins on the 2a sites (Supplementary Discussion 4 and Fig. 10). This behaviour is consistent with the $P6_3cm$ (B_2) magnetic symmetry, which forbids any linear magnetoelectric effect, but does allow nonlinear ones[8].

The most prominent feature in Fig. 3g is the pronounced divergence of the MeFM signal observed as the temperature is lowered in the intermediate-field A_2' ($P3c$) phase confined between 2 magnetoelectric anomalies: a kink and an asymmetric peak. These two anomalies are consistent with the two 'steps' in magnetization measurements (Supplementary Fig. 11), indicating a continuous spin reorientation transition in the A_2' region. The MeFM anomalies emerge only below ~6 K and converge to each other quickly as the temperature is lowered. The peak value at 2.8 K is 7–8 times larger than that of the linear magnetoelectric effect in the high-field A_2 phase.

The *T*–*H* phase diagram constructed from the MeFM peaks (red spheres) and the magnetization steps (blue triangles) is shown in Fig. 4a. The intermediate region (A_2' phase) becomes narrower at lower temperatures and seems to merge into a tri-critical point (black star), at which the order of the reorientation transition changes from second to first (the red dashed line indicates the first-order $B_2 \rightarrow A_2$ transition line). Such a phase diagram naturally emerges in the phenomenological Landau description of the reorientation transition (Fig. 4b and Supplementary Discussion 5). Importantly, the magnetoelectric response consists of two parts:

$$\left(\frac{\partial M_z}{\partial E_z}\right)_{E_z=0} = -\frac{\partial^2 f}{\partial E_z \partial H_z} + \frac{\partial^2 f/(\partial L_{A_2} \partial H_z) \times \partial^2 f/(\partial L_{A_2} \partial E_z)}{\partial^2 f/\partial L_{A_2}^2} \quad (1)$$

The first term describes the conventional response in the B_2 or A_2 phase, and the second term is the anomalous response resulting from the dependence of the magnetic order parameter L_{A_2} on applied **H** and **E** fields (see Supplementary Discussion 5 for details). The anomalous response is large in the continuous reorientation region (the A_2' phase), in which the magnetic state is extremely sensitive to external perturbations. It blows up near the tri-critical point where the system loses stiffness, $\partial^2 f/\partial L_{A_2}^2$, with respect to spin rotations (Supplementary Fig. 12). In other words, the diminishing energy barrier between B_2 and A_2 phases allows small perturbations such as **H** or **E** fields to swing the Mn^{3+} spins towards the A_2 phase by gaining either the Zeeman or the magnetoelectric free energy (Fig. 4c), resulting in an additional increase of the canting moment (M_z). This scenario is corroborated by the fact that in the vicinity of the tri-critical point not only the magnetoelectric, but also the magnetic susceptibility tends to diverge (Supplementary Fig. 11). The peak in the magnetoelectric response is remarkably well reproduced within our phenomenological theory (Fig. 3h and Supplementary Fig. 12).

In summary, we have demonstrated a direct visualization of magnetoelectric domains in multiferroic *h*-$ErMnO_3$ using newly developed MeFM. This technique provides a route for exploring emergent phenomena at the mesoscopic scale such as magnetoelectric coupling in multiferroic domains and domain walls[15–18,28–31], in multiferroic skyrmions[32], or in magnetic

© 2014 Macmillan Publishers Limited. All rights reserved

topological insulators[12,13,33]. Our results are in agreement with a microscopic model derived from first-principles calculations, providing compelling evidence of the new mechanism of magnetoelectric couplings mediated by lattice instability[4]. Furthermore, our MeFM results reveal a divergent magnetoelectric effect near the tricritical point, suggesting a possibility to enhance magnetoelectric effects by harnessing critical fluctuations.

Received 26 July 2013; accepted 17 October 2013; published online 1 December 2013

References

1. Ramesh, R. & Spaldin, N. A. Multiferroics: Progress and prospects in thin films. *Nature Mater.* **6,** 21–29 (2007).
2. Cheong, S. W. & Mostovoy, M. Multiferroics: A magnetic twist for ferroelectricity. *Nature Mater.* **6,** 13–20 (2007).
3. Spaldin, N. A., Cheong, S-W. & Ramesh, R. Multiferroics: Past, present, and future. *Phys. Today* **63,** 38–43 (2010).
4. Das, H., Wysocki, A. L., Geng, Y., Wu, W. & Fennie, C. J. Bulk magnetoelectricity in the hexagonal manganites and ferrites. Preprint at http://arxiv.org/abs/1302.1099 (2013).
5. Dzyaloshinskii, I. E. On the magneto-electrical effects in antiferromagnets. *Zh. Eksp. Teor. Fiz.* **37,** 881–882 (1959) (English translation in *Sov. Phys. JETP* **10,** 628–629).
6. Astrov, D. N. The magnetoelectric effect in antiferromagnetics. *Zh. Eksp. Teor. Fiz.* **38,** 984–985 (1960) (English translation in *Sov. Phys. JETP* **11,** 708–709).
7. Folen, V. J., Rado, G. T. & Stalder, E. W. Anisotropy of the magnetoelectric effect in Cr_2O_3. *Phys. Rev. Lett.* **6,** 607–608 (1961).
8. O'Dell, T. H. *The Electrodynamics of Magneto-Electric Media* (North-Holland, 1970).
9. Fiebig, M. Revival of the magnetoelectric effect. *J. Phys. D* **38,** R123–R152 (2005).
10. Kimura, T. *et al.* Magnetic control of ferroelectric polarization. *Nature* **426,** 55–58 (2003).
11. Hur, N. *et al.* Electric polarization reversal and memory in a multiferroic material induced by magnetic fields. *Nature* **429,** 392–395 (2004).
12. Essin, A. M., Moore, J. E. & Vanderbilt, D. Magnetoelectric polarizability and axion electrodynamics in crystalline insulators. *Phys. Rev. Lett.* **102,** 146805 (2009).
13. Qi, X-L. & Zhang, S-C. Topological insulators and superconductors. *Rev. Mod. Phys.* **83,** 1057–1110 (2011).
14. Borisov, P., Hochstrat, A., Shvartsman, V. V. & Kleemann, W. Superconducting quantum interference device setup for magnetoelectric measurements. *Rev. Sci. Instrum.* **78,** 106105 (2007).
15. Tokunaga, Y. *et al.* Composite domain walls in a multiferroic perovskite ferrite. *Nature Mater.* **8,** 558–562 (2009).
16. Choi, T. *et al.* Insulating interlocked ferroelectric and structural antiphase domain walls in multiferroic $YMnO_3$. *Nature Mater.* **9,** 253–258 (2010).
17. Tokunaga, Y., Taguchi, Y., Arima, T-h. & Tokura, Y. Electric-field-induced generation and reversal of ferromagnetic moment in ferrites. *Nature Phys.* **8,** 838–844 (2012).
18. Kagawa, F. *et al.* Dynamics of multiferroic domain wall in spin-cycloidal ferroelectric $DyMnO_3$. *Phys. Rev. Lett.* **102,** 057604 (2009).
19. Skumryev, V. *et al.* Magnetization reversal by electric-field decoupling of magnetic and ferroelectric domain walls in multiferroic-based heterostructures. *Phys. Rev. Lett.* **106,** 057206 (2011).
20. Geng, Y., Lee, N., Choi, Y. J., Cheong, S-W. & Wu, W. Collective magnetism at multiferroic vortex domain walls. *Nano. Lett.* **12,** 6055–6059 (2012).
21. Chung, T. K., Carman, G. P. & Mohanchandra, K. P. Reversible magnetic domain-wall motion under an electric field in a magnetoelectric thin film. *Appl. Phys. Lett.* **92,** 112509 (2008).
22. Katsufuji, T. *et al.* Dielectric and magnetic anomalies and spin frustration in hexagonal $RMnO_3$ (R = Y, Yb, and Lu). *Phys. Rev. B* **64,** 104419 (2001).
23. Van Aken, B. B., Palstra, T. T. M., Filippetti, A. & Spaldin, N. A. The origin of ferroelectricity in magnetoelectric $YMnO_3$. *Nature Mater.* **3,** 164–170 (2004).
24. Fennie, C. J. & Rabe, K. M. Ferroelectric transition in $YMnO_3$ from first principles. *Phys. Rev. B* **72,** 100103(R) (2005).
25. Artyukhin, S., Delaney, K. T., Spaldin, N. A. & Mostovoy, M. Landau theory of topological defects in multiferroic hexagonal manganites. *Nature Mater.* http://dx.doi.org/10.1038/nmat3786 (2013).
26. Yen, F. *et al.* Magnetic phase diagrams of multiferroic hexagonal $RMnO_3$ (R = Er, Yb, Tm, and Ho). *J. Mater. Res.* **22,** 2163–2173 (2007).
27. Chae, S. C. *et al.* Evolution of the domain topology in a ferroelectric. *Phys. Rev. Lett.* **110,** 167601 (2013).
28. Fiebig, M., Lottermoser, Th., Fröhlich, D., Goltsev, A. V. & Pisarev, R. V. Observation of coupled magnetic and electric domains. *Nature* **419,** 818–820 (2002).
29. Lottermoser, T. *et al.* Magnetic phase control by an electric field. *Nature* **430,** 541–544 (2004).
30. Wang, W. *et al.* Room-temperature multiferroic hexagonal $LuFeO_3$ films. *Phys. Rev. Lett.* **110,** 237601 (2013).
31. Sugie, H., Iwata, N. & Kohn, K. Magnetic ordering of rare earth ions and magnetic-electric interaction of hexagonal $RMnO_3$ (R = Ho, Er, Yb or Lu). *J. Phys. Soc. Jpn* **71,** 1558–1564 (2002).
32. Seki, S., Ishiwata, S. & Tokura, Y. Magnetoelectric nature of skyrmions in a chiral magnetic insulator Cu_2OSeO_3. *Phys. Rev. B* **86,** 060403(R) (2012).
33. Chang, C-Z. *et al.* Experimental observation of the quantum anomalous hall effect in a magnetic topological insulator. *Science* **340,** 167–170 (2013).

Acknowledgements

We thank D. Vanderbilt, K. Rabe, S. Artyukhin, P. Chandra and P. Coleman for helpful discussions. Research at Rutgers was supported by the US DOE-BES under Award # DE-SC0008147 (PFM and MeFM studies), and by the NSF under award # DMR-1104484 (synthesis and characterization). Y.G. and W.W. were partially supported by the NSF under award # DMR-0844807. A.L.W. was supported by the Cornell Center for Materials Research with funding from NSF MRSEC program, cooperative agreement DMR-1120296. H.D. and C.J.F. was supported by the DOE-BES under Award Number DE-SCOO02334. M.M. was supported by FOM grant 11PR2928 and the Niels Bohr International Academy.

Author contributions

W.W. conceived and designed the project. S-W.C. and X.W. grew and annealed *h*-$ErMnO_3$ crystals and characterized the magnetic properties. Y.G. carried out PFM and MeFM measurements and analysed the data. A.L.W., H.D. and C.J.F. performed first-principles calculations and developed a phenomenological theory of the linear magnetoelectric effect. M.M. performed the phenomenological Landau theory symmetry analysis of the linear magnetoelectric and the anomalous magnetoelectric response. Y.G., C.J.F., M.M. and W.W. wrote the manuscript with input from all authors. Y.G., A.L.W., M.M. and W.W. wrote the Supplementary Information. All authors participated in discussions.

Additional information

Supplementary information is available in the online version of the paper. Reprints and permissions information is available online at www.nature.com/reprints. Correspondence and requests for materials should be addressed to W.W.

Competing financial interests

The authors declare no competing financial interests.

© 2014 Macmillan Publishers Limited. All rights reserved